

## Resolution for radar and x-ray tomography

Frank Natterer<sup>1</sup>, Margaret Cheney<sup>2</sup> and Brett Borden<sup>3</sup>

<sup>1</sup> Institut für Numerische und Instrumentelle Mathematik, University of Münster,  
48149 Münster, Germany

<sup>2</sup> Department of Mathematical Sciences, Rensselaer Polytechnic Institute, Troy, NY 12180, USA

<sup>3</sup> Physics Department, Naval Postgraduate School, Monterey, CA 93943-5001, USA

Received 23 April 2003, in final form 2 July 2003

Published 12 November 2003

Online at [stacks.iop.org/IP/19/S55](http://stacks.iop.org/IP/19/S55)

### Abstract

Radar imaging and x-ray computed tomography (CT) are both based on inverting the Radon transform. Yet radar imaging can make images from as little as two degrees of aperture while x-ray CT typically requires an aperture of at least  $120^\circ$ . Our discussion addresses this phenomenon.

(Some figures in this article are in colour only in the electronic version)

### 1. Introduction

Although the mathematical similarities between x-ray computed tomography (CT) and synthetic aperture radar image processing (either Spotlight SAR or ISAR) have been recognized for several decades [3, 4], the connection between the two disciplines is often surprising even to seasoned practitioners in these fields. The relationship is, perhaps, unexpected because of the fundamental differences in the acquired data. Radar data are usually electromagnetic field measurements of echo pulses with relatively long wavelength. X-ray data consist of high-frequency transmission measurements. Moreover, radar systems are generally coherent (they record the pulse-to-pulse relative phase) while x-ray systems are generally incoherent.

In both cases, the limited-aperture problem is of paramount practical importance. And it is in this restricted-data environment that a surprising *distinction* between the two imaging problems can be found: good-quality x-ray tomographic images typically demand significantly larger measurement apertures than are required by their radar counterparts (in practice, as much as a factor of 50 larger).

In what follows, we will examine this phenomenon and show that the concept of *carrier frequency* is different for the two types of measurement systems. In radar, the transmitted waveform is modulated by a frequency chosen to conform with atmospheric ‘windows’ and engineering (bandwidth-generation) considerations [1]. In x-ray systems, the notion that corresponds to the radar carrier frequency is a certain spatial frequency that arises from the size and spacing of the sources and detectors at each view.

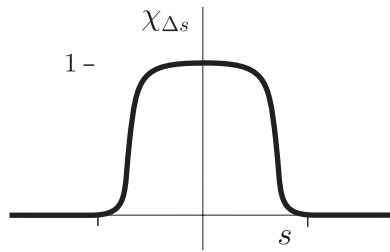


Figure 1. Graph of a typical detector response function.

Our discussion will not require an in-depth understanding of either radar or x-ray imaging techniques. We will begin by establishing the notation and briefly demonstrating how the two methods are related. Section 3 contains our principal result and examines the nature of the resolution cell for each type of imaging system. We will also illustrate our results with some (synthetic) examples.

## 2. Imaging

### 2.1. X-ray imaging

In x-ray imaging we measure line integrals of a real-valued density function  $f$  in  $\mathbb{R}^2$ . These line integrals are conveniently modelled by the Radon transform:

$$(Rf)(\boldsymbol{\theta}, s) = \int_{\mathbb{R}^2} \delta(s - \boldsymbol{\theta} \cdot \boldsymbol{x}) f(\boldsymbol{x}) d\boldsymbol{x}, \quad (2.1)$$

where  $\boldsymbol{\theta} = (\cos \varphi, \sin \varphi)^T \in S^1$  and  $s \in \mathbb{R}^1$ ; see e.g. [5]. The vector  $\boldsymbol{\theta}$  denotes the direction perpendicular to the lines of integration and, in limited angle tomography,  $\boldsymbol{\theta}$  is restricted to the sector  $|\varphi| \leq \Phi$ .

If we had a continuum of infinitely small detectors we would measure (2.1). In the finite-sized detector case, we measure a band-limited version

$$(R_b f)(\boldsymbol{\theta}, s_i) = \int (Rf)(\boldsymbol{\theta}, s) \chi_{\Delta s}(s - s_i) ds \quad (2.2)$$

where  $\chi_{\Delta s}$  is the detector response function. An idealized model would be

$$\chi_{\Delta s} = \begin{cases} 1 & \text{on detector} \\ 0 & \text{off detector,} \end{cases} \quad (2.3)$$

but in practice  $\chi_{\Delta s}$  looks more like figure 1.

The Fourier transform of  $\chi_{\Delta s}$  is effectively supported in some region around zero, say  $(-b, b)$ , where, in accordance with the sampling theorem,  $b \sim \pi/\Delta s$ . Since  $f$  is real valued we can ignore negative frequencies, restricting the frequency range of  $\chi_{\Delta s}$  to  $[0, b)$ . This makes the comparison with radar data easier.

It follows that x-ray data are sampled versions of (2.2):

$$d(\boldsymbol{\theta}, s) = (R_b f)(\boldsymbol{\theta}, s) = ((Rf)(\boldsymbol{\theta}, \cdot) * \chi_{\Delta s})(s). \quad (2.4)$$

## 2.2. Radar imaging

It is shown in [2] and [1] that under the start–stop approximation, the data from band-limited high-range-resolution (HRR) pulses obey

$$\begin{aligned}
 \eta(\boldsymbol{\theta}, t) &= \int f(\mathbf{x}) \int_{\omega_1}^{\omega_2} e^{i\omega(t-\boldsymbol{\theta}\cdot\mathbf{x})} d\omega d\mathbf{x} \\
 &= \int f(\mathbf{x}) \delta(s - \boldsymbol{\theta} \cdot \mathbf{x}) \int_{\omega_1}^{\omega_2} e^{i\omega(t-s)} d\omega ds d\mathbf{x} \\
 &= \int (Rf)(\boldsymbol{\theta}, s) \int_{\omega_1}^{\omega_2} e^{i\omega(t-s)} d\omega ds \\
 &= [(Rf)(\boldsymbol{\theta}, \cdot) * \chi](t),
 \end{aligned} \tag{2.5}$$

where

$$\chi(s) = \int_{\omega_1}^{\omega_2} e^{i\omega s} d\omega. \tag{2.6}$$

Obviously the Fourier transform of  $\chi$  is supported in the interval  $(\omega_1, \omega_2)$ . The *bandwidth*  $b = \omega_2 - \omega_1$  plays the same role as  $b$  introduced in the discussion of x-ray imaging.

## 2.3. Comparison

In both cases, the data are of the form

$$d(\boldsymbol{\theta}, \cdot) = (Rf)(\boldsymbol{\theta}, \cdot) * \chi \tag{2.7}$$

for a function  $\chi$  with finite bandwidth. The key difference is that for x-ray imaging, the  $\chi$  frequency band is  $(0, b)$ , whereas for radar imaging, the  $\chi$  frequency band is centred about a (usually high) central frequency  $\omega_c = \frac{1}{2}(\omega_1 + \omega_2)$ .

To express the fact that in both problems we have only a limited angular aperture, we multiply the data by an angular cut-off function

$$\chi_\Phi(\boldsymbol{\theta}) = \begin{cases} 1 & \text{for } \boldsymbol{\theta} \text{ with } |\varphi| \leq \Phi \\ 0 & \text{otherwise.} \end{cases} \tag{2.8}$$

The data, then, are

$$D(\boldsymbol{\theta}, s) = \chi_\Phi(\boldsymbol{\theta})[(Rf)(\boldsymbol{\theta}, \cdot) * \chi](s). \tag{2.9}$$

For simplicity we ignore the issue of angular sampling, since it is similar for both x-ray and radar imaging.

## 3. Resolution analysis

For the resolution analysis, we begin by Fourier transforming (2.9) from  $s$  into  $\omega$ . This gives us

$$\hat{D}(\boldsymbol{\theta}, \omega) = \chi_\Omega(\boldsymbol{\theta}) \widehat{Rf}(\boldsymbol{\theta}, \omega) \hat{\chi}(\omega). \tag{3.10}$$

Then we use the projection-slice theorem, which states that  $\widehat{Rf}(\boldsymbol{\theta}, \omega) = \hat{f}(\omega\boldsymbol{\theta})$ . Here  $\widehat{Rf}$  denotes the one-dimensional Fourier transform ( $s \rightarrow \omega$ ) and  $\hat{f}$  denotes the two-dimensional Fourier transform. Applying this theorem, we can write the  $s$ -Fourier transform of the data as

$$\hat{D}(\boldsymbol{\theta}, \omega) = \hat{K}(\omega\boldsymbol{\theta}) \hat{f}(\omega\boldsymbol{\theta}), \tag{3.11}$$

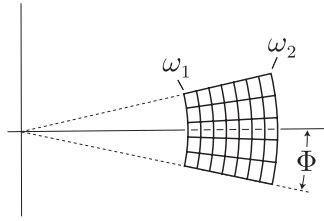


Figure 2. Sector in theta-omega space.

where

$$\hat{K}(\omega\theta) = \chi_{\Phi}(\theta)\hat{\chi}(\omega) \quad (3.12)$$

is one in the shaded region shown in figure 2 and zero elsewhere.

If  $f$  has compact support, then since  $\hat{f}$  is an entire function,  $\hat{f}$  is uniquely determined by the data in the sector presented in figure 2. This implies that  $f$  is uniquely determined by the data in both the radar and x-ray cases. Exact reconstruction, however, requires analytic continuation, which is hopelessly unstable in this case. Therefore, ‘resolution’ refers to stable reconstruction procedures. In fact, we restrict ourselves to reconstruction in the minimum norm sense, i.e., our reconstruction is obtained simply by putting the Fourier transform of  $f$  to zero outside the measured region and then computing the inverse transform. Equivalently we could use a filtered backprojection algorithm in the limited angular range.

The minimal-norm reconstruction  $f_R$  of  $f$  is obtained from

$$\hat{f}_R = \hat{K}\hat{f} = \hat{D}, \quad (3.13)$$

or, after inverse transforming,  $f_R = K * f$ . The point-spread function  $K$  is

$$K(x) = \int_{|\xi|=\omega_1}^{|\xi|=\omega_2} \int_{-\Phi}^{\Phi} e^{ix \cdot \xi} d\xi, \quad (3.14)$$

and can be calculated by writing

$$x = r(\cos \psi, \sin \psi) \quad \text{and} \quad \xi = \omega(\cos \phi, \sin \phi) \quad (3.15)$$

so that  $x \cdot \xi = \omega r \cos(\phi - \psi)$ . For the radar problem, the ‘down-range’ direction corresponds to  $\psi = 0$  and ‘cross-range’ corresponds to  $\psi = \pi/2$ . For radar, the small-angle approximation is  $\cos \phi \approx 1$  and  $\sin \phi \approx \phi$ .

In the x-ray case,  $\psi = 0$  corresponds to the direction perpendicular to the lines and  $\psi = \pi/2$  corresponds to the direction along the lines. For ease of exposition we also adopt the radar jargon for the x-ray case.

### 3.1. Down-range resolution

For  $\psi = 0$ , under the small-angle approximation, we obtain for (3.14)

$$\begin{aligned} K(r, 0) &\approx \int_{\omega_1}^{\omega_2} \omega \int_{-\Phi}^{\Phi} e^{i\omega r} d\phi d\omega \\ &= 2\Phi \int_{\omega_1}^{\omega_2} \omega e^{i\omega r} d\omega \\ &= \frac{2\Phi}{i} \frac{d}{dr} \int_{\omega_1}^{\omega_2} e^{i\omega r} d\omega \\ &= \frac{2\Phi}{i} \frac{d}{dr} \left[ e^{i\omega_2 r} \frac{1}{2} b \operatorname{sinc} \frac{1}{2} br \right]. \end{aligned} \quad (3.16)$$

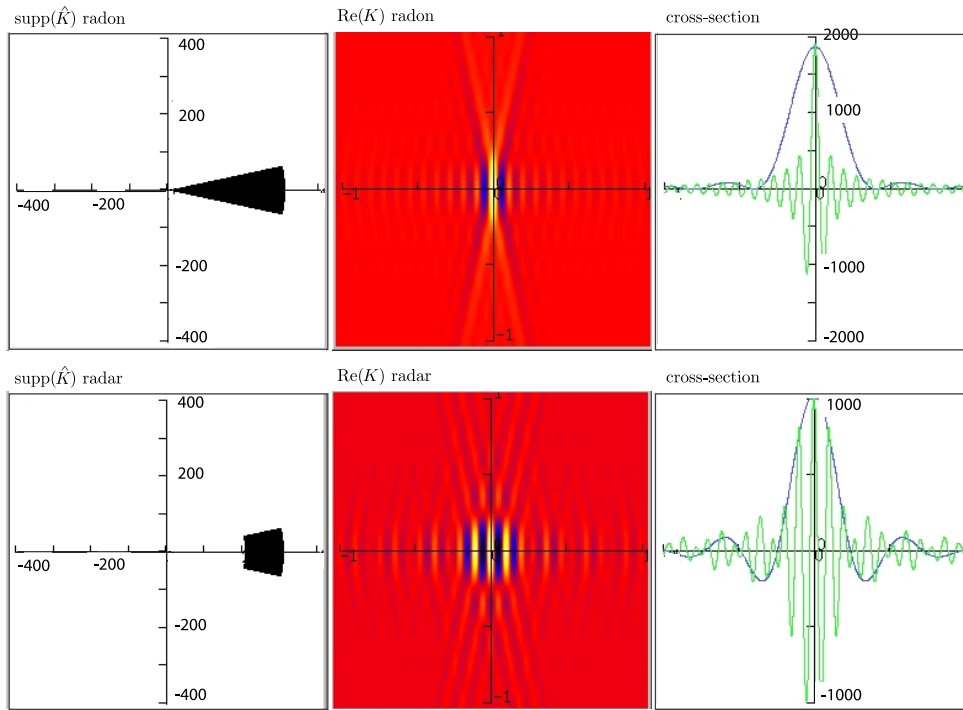


**Figure 3.** From left to right:  $\text{supp}(\hat{K})$ ,  $\text{Re } K$ , cross sections (fast oscillating horizontal, slowly oscillating vertical) through  $\text{Re } K$  for x-ray (top) and radar (bottom). The down range is horizontal.

In the x-ray case, the centre frequency  $\omega_c$  is  $b/2$  and we obtain

$$\begin{aligned} \text{Re } K(r, 0) &\approx \phi b \frac{d}{dr} \left[ \sin \frac{1}{2} br \text{sinc} \frac{1}{2} br \right] \\ &= \frac{\Phi b}{2} \frac{d}{dr} \left[ \frac{1 - \cos br}{\frac{1}{2} br} \right] \end{aligned} \quad (3.17)$$

$$= \phi b^2 (\text{sinc } br - \frac{1}{2} (\text{sinc } \frac{1}{2} br)^2), \quad (3.18)$$

where we have used the identity  $\sin^2(A/2) = (1 - \cos A)/2$ . We see that  $\text{Re } K(r, 0)$  looks like a sinc function with the main lobe slightly narrower than  $2\pi/b$ . (See the rightmost column of figure 3 for a plot.) Consequently, the down-range resolution is  $2\pi/b$ .

In the radar case, where  $\omega_c \gg b$ , the leading order term of (3.16) is obtained by differentiating the exponential

$$K(r, 0) \approx b\omega_c \Phi e^{i\omega_c r} \text{sinc } \frac{1}{2} br, \quad (3.19)$$

yielding down-range resolution  $4\pi/b$ . (See the rightmost column of figure 3 for a plot.) In (3.19), it is the sinc function that governs the resolution. However, the oscillatory factor  $\exp(i\omega_c r)$ , which is the cause of the scintillation effect [1], is a major problem for reconstructing the smooth function; see our discussion in what follows.

**Table 1.** Resolution for the radar and x-ray cases. Numerical values correspond to figure 3, i.e.,  $\Phi = 12^\circ$ ,  $\omega_c = 250$ ,  $b = 100$  for radar,  $b = 300$  for x-ray.

	Resolution	
	Cross-range	Down-range
Radar	$2\pi/(\omega_c \Phi)$ 0.120	$4\pi/b$ 0.126
X-ray	$4\pi/(b\Phi)$ 0.200	$2\pi/b$ 0.0209

### 3.2. Cross-range resolution

When  $\psi = \pi/2$ , we have  $\cos(\phi - \psi) = \sin \phi$ , which, under the small-angle approximation, is approximately  $\phi$ . With this approximation, the computation of (3.14) is

$$\begin{aligned}
 K(0, r) &\approx \int_{\omega_1}^{\omega_2} \omega \int_{-\Phi}^{\Phi} e^{i\omega r \phi} d\phi d\omega \\
 &= \int_{\omega_1}^{\omega_2} \omega \frac{e^{i\omega r \Phi} - e^{-i\omega r \Phi}}{i\omega r} d\omega \\
 &= \frac{1}{2ir} [e^{i\omega_c r \Phi} b \operatorname{sinc}(\frac{1}{2}br\Phi) - e^{-i\omega_c r \Phi} b \operatorname{sinc}(\frac{1}{2}br\Phi)] \\
 &= b\omega_c \Phi \operatorname{sinc}(\frac{1}{2}br\Phi) \operatorname{sinc}(\omega_c r \Phi).
 \end{aligned} \tag{3.20}$$

In the radar case, with  $\omega_c \gg b$ , we have

$$K(0, r) \approx b\omega_c \Phi \operatorname{sinc}(\omega_c r \Phi) \tag{3.21}$$

while in the x-ray case  $\omega_c = b/2$ , so that

$$K(0, r) \approx b^2 \phi (\operatorname{sinc} \frac{1}{2}br\Phi)^2. \tag{3.22}$$

Thus we have cross-range resolution  $2\pi/(\omega_c \Phi)$  in the radar case and  $4\pi/(b\Phi)$  in the x-ray case. Our results are compiled in table 1.

### 3.3. Numerical examples

We computed  $K$  numerically for  $\phi = 12^\circ$ ,  $\omega_1 = 200$  and  $\omega_2 = 300$ , (i.e.<sup>4</sup>,  $\omega_c = 250$ ,  $b = 100$  for the radar case and  $b = 300$  for x-ray case). These results are plotted in figure 3. The results clearly corroborate our analysis.

So far we have discussed resolution as defined by the width of the main peak in the *magnitude* of the point-spread function  $K$ . This main peak defines a *resolution cell*, which is a rectangle whose sides have the lengths of the main lobes of  $K$  in the down-range and cross-range directions, respectively. Considering the magnitude of  $K$  is sufficient for objects  $f$  that consist of point scatterers, i.e., objects for which

$$f(\mathbf{x}) = \sum_{\ell=1}^P f_\ell \delta(\mathbf{x} - \mathbf{x}_\ell). \tag{3.23}$$

<sup>4</sup> We note that the choice of  $\omega_c = 250$  in the radar case does not mean that we are using 250 Hz frequency. This is a scaled frequency whose value depends on factors such as the wavelength-to-scatterer ratio, atmospheric windows and size constraints on the antenna;  $\omega_c = 250$  is reasonable in certain situations.

In this case, our reconstruction is

$$(K * f)(\mathbf{x}) = \sum_{\ell=1}^P f_{\ell} K(\mathbf{x} - \mathbf{x}_{\ell}). \quad (3.24)$$

If the resolution cells centred at  $x_{\ell}$  and  $x_k$  do not overlap for  $\ell \neq k$ , then the sum in (3.24) has only one term that is significantly different from 0, and

$$|(K * f)(\mathbf{x})| \approx \sum_{\ell=1}^P |f_{\ell}| |K(\mathbf{x} - \mathbf{x}_{\ell})|. \quad (3.25)$$

Here, the down-range oscillations in  $K$  disappear by taking absolute values, and  $|K|$  behaves very much as if the oscillations due to the factor  $\exp(i\omega_c r)$  were absent. It follows that the scatterers at  $x_{\ell}$  appear separated if the resolution cells do not overlap. Table 1 is based on this reasoning.

The situation changes drastically if extended objects are considered, i.e., if  $f$  is a piecewise smooth function. Our point-spread functions are of the form

$$K(\mathbf{x}) = e^{i\omega_c x_1} K_0(\mathbf{x}) \quad (3.26)$$

where  $\mathbf{x} = (x_1, x_2)^T$ ,  $x_1$  is the down-range variable,  $x_2$  the cross-range variable and  $K_0$  is significantly different from 0 only in the resolution cell centred at the origin. Then our reconstruction can be written

$$(K * f)(\mathbf{x}) = \int_{\mathbb{R}^2} e^{i\omega_c(x_1 - y_1)} K_0(\mathbf{x} - \mathbf{y}) f(\mathbf{y}) d\mathbf{y}. \quad (3.27)$$

If  $f$  is smooth in the resolution cell centred at  $\mathbf{x}$ , then this integral is negligible for large  $\omega_c$ . Thus, smooth parts of the object cannot be seen. If  $f$  is a smooth curve-like object (i.e.,  $f$  is of the form  $f(\mathbf{y})\delta(\mathbf{y} - \Gamma)$  with  $f$  smooth on the smooth curve  $\Gamma \subseteq \mathbb{R}^2$ ) then the reconstruction is

$$(K * f)(\mathbf{x}) = \int_{\Gamma} e^{i\omega_c(x_1 - y_1)} K_0(\mathbf{x} - \mathbf{y}) f(\mathbf{y}) ds(\mathbf{y}). \quad (3.28)$$

If  $\Gamma$  is smooth in the resolution cell centred at  $\mathbf{x}$ , and if the direction of (the tangent to)  $\Gamma$  is not cross range, then  $\Gamma$  can be represented by  $y_2 = g(y_1)$  with a smooth function  $g$ , and the reconstruction is

$$(K * f)(\mathbf{x}) = \int_{\mathbb{R}^1} e^{i\omega_c(x_1 - y_1)} K_0(x_1 - y_1, x_2 - g(y_1)) f(y_1, g(y_1)) \sqrt{1 + |g'(y_1)|^2} dy_1. \quad (3.29)$$

Again, this is negligible for large  $\omega_c$ . However, if  $\Gamma$  has cross-range direction at  $\mathbf{x}$ , i.e., if  $\Gamma$  is represented by  $y_1 = x_1$ , then

$$(K * f)(\mathbf{x}) = \int_{\mathbb{R}^1} K_0(0, x_2 - y_2) f(x_1, y_2) dy_2, \quad (3.30)$$

and this may be quite large, independent of  $\omega_c$ . Points on curves with cross-range direction are called *specular*. We conclude that specular points show up conspicuously in the reconstructed image. However, since the measurements associated with a specular flash are typically supported on an aperture  $\ll \Phi$ , the cross-range resolution of the specular target element will be correspondingly reduced.

Finally, we consider the case where  $\mathbf{x}$  is a corner of  $\Gamma$ . Using integration by parts one can show that, generically,

$$(K * f)(\mathbf{x}) = O\left(\frac{1}{\omega_c}\right). \quad (3.31)$$

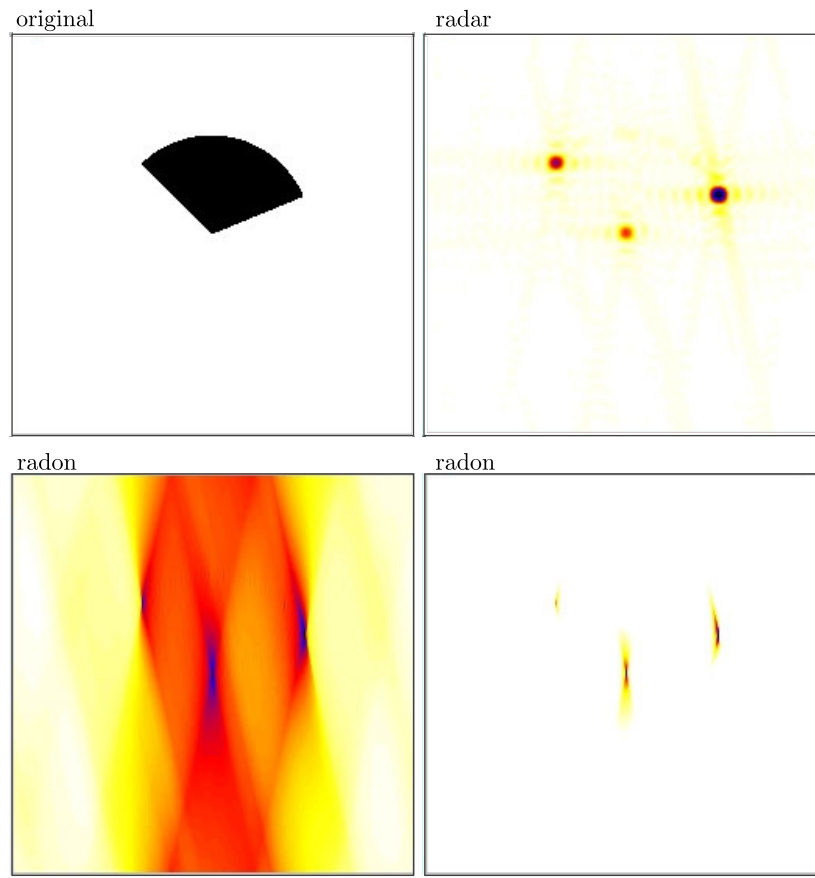


**Figure 4.** Circular section (top left). Reconstruction from radar data (top right), x-ray data without (bottom left) and with (bottom right) thresholding.

This is not as big as the contribution of the specular points, but it is much larger than the contribution from the smooth parts of the object.

What has been said for  $\omega_c \gg b$  (radar) also applies, by and large, to the case  $\omega_c = b/2$  (x-ray). The reason for this is that in the latter case  $K$  is also oscillating in the down-range direction.

Using the same parameter values as given in figure 3 we reconstructed the circular sector presented in the top left of figure 4. The reconstruction in the radar case (top right) shows the corners with the same resolution in the down-range and cross-range directions, as predicted by table 1. The bottom left part of figure 4 shows the reconstruction for the x-ray case. The corners can be identified in an otherwise inconclusive picture. After thresholding (bottom right) the corners emerge in accordance with table 1—in particular, with a much better down-range than cross-range resolution.

#### 4. Discussion

In summary, we can state that small-synthetic-aperture radar and small-angle tomography share some essential features. In both cases we can reconstruct only point scatterers,

corners and specular points, the other features of the object remaining invisible. We remark in passing that this is in agreement with results obtained by microlocal analysis [6], and indeed provides a justification for the use of high-frequency asymptotics in limited-aperture problems.

The cross-range resolution can be made arbitrarily fine by choosing  $\omega_c$  (radar) and  $b$  (x-ray) sufficiently large. The down-range resolution depends, in both cases, on the bandwidth and is considerably better in the x-ray case ( $2\pi/\omega_2$ ) than in the radar case ( $4\pi(\omega_2 - \omega_1)$ ) for the same maximal frequency  $\omega_2$ . This advantage of the x-ray case over the radar one seems to be the only benefit of having data extending down to  $\omega = 0$  rather than  $\omega = \omega_1 > 0$ .

### Acknowledgments

This work was supported by the Office of Naval Research, and by the Air Force Office of Scientific Research<sup>5</sup> under agreement number F49620-03-1-0051. This work was also partially supported by CenSSIS, the Center for Subsurface Sensing and Imaging Systems, under the Engineering Research Centers Program of the National Science Foundation (award number EEC-9986821) and by the NSF Focused Research Groups in the Mathematical Sciences program.

### References

- [1] Borden B 2002 Mathematical problems in radar inverse scattering *Inverse Problems* **18** R1–28
- [2] Cheney M and Borden B 2003 Microlocal structure of inverse synthetic aperture radar data *Inverse Problems* **19** 173–94
- [3] Mensa D L, Halevy S and Wade G 1983 Coherent Doppler tomography for microwave imaging *Proc. IEEE* **71** 254
- [4] Munson D C, O'Brien D and Jenkins W K 1983 A tomographic formulation of spotlight mode synthetic aperture radar *Proc. IEEE* **71** 917
- [5] Natterer F 1986 *The Mathematics of Computerized Tomography* (New York: Wiley)
- [6] Quinto E T 1993 Singularities of the x-ray transform and limited data tomography in  $\mathbb{R}^2$  and  $\mathbb{R}^3$  *SIAM J. Math. Anal.* **24** 1215–25

<sup>5</sup> Consequently the US Government is authorized to reproduce and distribute reprints for Governmental purposes notwithstanding any copyright notation thereon. The views and conclusions contained herein are those of the authors and should not be interpreted as necessarily representing the official policies or endorsements, either expressed or implied, of the Air Force Research Laboratory or the US Government.